Measurements of Skin-friction of Systematically Generated Surface Roughness

Julio M. Barros[a,*], Michael P. Schultz[b], Karen A. Flack[c]

[a] *Fluid Mechanics Unit, Okinawa Institute of Science and Technology, 1919-1 Tancha, Onna-son, Okinawa - 904-0945 Japan*
[b] *Department of Naval Architecture and Ocean Engineering, United States Naval Academy, Annapolis, MD - 21402 USA*
[c] *Department of Mechanical Engineering, United States Naval Academy, Annapolis, MD - 21402 USA*

Abstract

The flow conditions at which a given surface will begin to show the effects of roughness in the form of increased wall shear stress above that of the hydraulically-smooth wall and the behavior of frictional drag in the transitionally-rough regime are still poorly understood. From a practical standpoint, the engineering correlations to predict this behavior should be based on information that can be obtained solely from the surface topography, thus excluding any information that requires hydrodynamic testing. The goal of this work is to take a systematic approach when generating surface roughness where the roughness parameters can be controlled. Three surfaces with fixed amplitude and varying power-law spectral slope ($E(\kappa) \sim \kappa^P$; $P = -0.5, -1.0, -1.5$) were generated and replicated using high-resolution 3D printing. Results show that the surface with the shallower spectral slope, $P = -0.5$, produces the highest drag, whereas the surface with the steeper spectral slope, $P = -1.5$ produces the least drag. This highlights that some roughness scales do not contribute significantly to the drag. In fact, the effective slopes, ES of the investigated surfaces were less than 0.35, which indicates that the surfaces are in the so-called "wavy" regime (Schultz and Flack, 2009). A high-pass filter of 1 mm (corresponding to ~ 10 times of the roughness height) was applied. By removing the long-wavelength roughness scales, the correlation between the filtered roughness amplitude and the frictional drag showed the correct trend.

Keywords: random roughness, friction factor, rough-wall turbulent flow, channel flow

1. Introduction

Surface roughness is encountered in a multitude of practical and industrial applications, such as flow inside pipelines or over turbine blades (which may degrade with deployment time), and flow over complex geometries and/or topographies, such as urban and environmental flows. It is widely known that roughness increases frictional drag, which may lead to higher thermal loads and degradation of performance. Recently tested roughness was seen to cause additional undesirable effects in certain conditions, such as secondary flow (Barros and Christensen, 2014; Kevin et al., 2017; Anderson et al., 2015; Nugroho et al., 2013), which may lead to lateral drag (Willingham et al., 2014). Given the complexity of rough-wall flows, it is often desired to develop simple predictive models for frictional drag that can provide a good degree of accuracy in practical engineering applications. Such a model can be derived purely from the surface topography (i.e., roughness statistics, such as, root-mean-square, *r.m.s.*, skewness, Sk, kurtosis, Ku, etc.). Therefore, it is crucial to understand the relationship between surface's topography and its impact on the hydraulic resistance. One example would be the characterization of drag penalties due to different biofouling conditions on ship hulls. A particular advantage for having a simple drag predictive model based upon the roughness statistics would be the optimization between drag penalties (and thus a reduction in ship's performance and cruising speeds) and fuel/cleaning costs.

Many important studies have been conducted on simplified, sparse arrays of roughness elements, such as cubes and transverse square bars, which often have a single roughness scale, in order to develop correlations between drag penalties (more specifically, the roughness function, ΔU^+) and some roughness parameters. These parameters range from simple ones, such as roughness spacing parameter, λ = pitch/height (Bettermann, 1965) and the density parameter, λ_d = total surface area/total roughness area (Dvorak, 1969), to more complex ones, such as the combined density and shape parameter, $\Lambda = (d/k)(A_f/A_s)^{-4/3}$, where d is average element spacing, k is the roughness height, A_f is the frontal area of a single roughness element, and A_s is the windward wetted surface area of a single roughness element (Dirling, 1973). Macdonald et al. (1998) introduced an analytical model to predict drag, in the form of surface roughness height, z_0 (similar to the equivalent sand-grain roughness height, k_s), for staggered and square arrays of cubes. This model agrees very well with experimental data for a wide range of planform densities, $\lambda_p = A_p/A_d$, where

*Corresponding author
Email addresses: juliomanuel.barrosjunior@oist.jp (Julio M. Barros), mschultz@usna.edu (Michael P. Schultz), flack@usna.edu (Karen A. Flack)
https://doi.org/10.1016/j.ijheatfluidflow.2018.04.015

A_p is the total plan area and A_d it the total area covered by the roughness elements. Recently, Yang et al. (2016) proposed a new analytical model for cubes (staggered and square arrays), where an exponential mean velocity profiles is assumed in the roughness sublayer, as evidenced in LES results presented in their work. Additionally, this model takes into account volumetric sheltering effects due to the momentum deficit in the wake of the roughness elements, which is accounted for in the drag on adjacent elements. Good agreement was found between their LES results and the Macdonald et al. (1998) analytical model.

As was previously mentioned, many practical roughness topographies embody a multitude of roughness scales, and therefore cannot be easily characterized by the parameters described above. In addition, these practical, realistic roughness types usually cover the entire surface, which, again, limit the use of parameters based on element to element spacing. Therefore, it seems that any predictive model for the frictional drag on these realistic surfaces should rely upon surface statistics. Flack and Schultz (2010), using a multitude of roughness geometries ranging from sandpaper with various grit scales to pyramids and packed spheres, developed a predictive model for k_s that is solely based upon the roughness root-mean-square height, k_{rms}, and the skewness of the probability density function, Sk, in the form of,

$$k_{s,\text{ predicted}} = A\, k_{rms}(1 + Sk)^b \tag{1}$$

where A and b are determined from a least square fit. It should be noted that this model is only applicable in the fully-rough regime. If fact, developing a model that covers all regimes - that is, hydraulically-smooth to transitionally-rough and fully-rough regimes, has proven to be challenging. Flack et al. (2016) generated 15 surfaces via grit-blasting, with various media sizes and combinations of thereof, and the skin friction was measured for a wide range of Reynolds numbers, covering all roughness regimes. They showed that the roughness function, ΔU^+ remains largely invariant with surface texture. One possible reason why these surfaces did not display significant differences in the transitionally-rough regime could be linked to Sk, which for all the tested surfaces were inherently negative. Additionally, the authors verified that k_s correlated quite well with k_{rms} and Sk.

Based upon the work from Flack et al. (2016), the current work takes a more systematic approach, which consists of mathematically generating surfaces roughness where the roughness statistical parameters can be controlled. Three surface were created where the amplitude of the roughness was nominally kept constant coupled with a systematic variation in the power-spectral density. The reproduction of these surfaces was done via high-resolution 3D printing, and subsequent hydrodynamics tests were performed in a channel flow facility where the skin-friction was measured.

2. Experimental Facilities and Methods

The present experiments were conducted in the high Reynolds number turbulent channel flow facility at the United States Naval Academy. The test section is 25 mm in height (H), 200 mm in width (W), and 3.1 m in length (L). The channel flow facility has a reservoir tank containing 4000 L of water. The water temperature is held constant to within $\pm 0.25°$ C using a thermostat-controlled chiller. The water is deaerated and filtered to remove particulate material larger than 2 μm. The flow is driven by two 7.5 kW pumps operated in parallel. The pumps are operated by separate, variable frequency drive units which are computer-controlled. The flow rate is measured using a Yokogawa ADMAG AXF magnetic flow-meter that has an accuracy of 0.2% of the reading. The bulk mean velocity in the test section ranges from 0.4 - 11.0 m/s, resulting in a Reynolds number based on the channel height and bulk mean velocity (Re_m) range from 10,000 - 300,000. Further details of the facility including flow management devices, tripping, and flow quality are given in Schultz and Flack (2013).

Nine static pressure taps are located in the test section of the channel. They are 0.75 mm holes and are placed along the centerline of the side wall of the channel and are spaced $6.8H$ apart. The streamwise pressure gradient (dp/dx) is determined with a GE-Druck LPM 9000 series differential pressure transducer with a 100 mbar range, and have an accuracy of $\pm 0.1\%$ of full scale. Pressure taps 5 - 8 are used to measure the streamwise pressure gradient in the channel, located $\sim 90H$ - $110H$ downstream of the trip at the inlet to the channel. The linearity in the measured pressure gradient using these four taps was quite good with a coefficient of determination (R^2) of the regression generally greater than 0.995.

The wall shear stress, τ_w, is determined via measurement of the streamwise pressure gradient given as follows:

$$\tau_w = -\frac{H}{2}\frac{dp}{dx} \tag{2}$$

or expressed as the skin-friction coefficient, C_f

$$C_f = \frac{\tau_w}{\frac{1}{2}\rho U^2} = 2\Big(\frac{u_\tau}{U}\Big)^2 \tag{3}$$

where H = channel height, p = static pressure, x = streamwise distance, ρ = fluid density, U = bulk mean velocity, and u_τ = friction velocity. A similarity-law procedure of Granville (1987) for fully-developed internal flows was employed to determine the roughness function, ΔU^+. Granville's method states that the roughness function can be obtained by:

$$\Delta U^+ = U_s^+ - U_r^+ = \sqrt{\frac{2}{C_{f_S}}} - \sqrt{\frac{2}{C_{f_R}}} \tag{4}$$

where the subscripts S and R represents smooth and rough surfaces, respectively, evaluated at the same $Re_m(C_f)^{\frac{1}{2}}$ or Re_τ.

© 2018

This work is licensed under a Creative Commons "Attribution-NonCommercial-NoDerivatives 4.0 International" license.

The flow develops over smooth walls for a distance of $60H$ in the upstream portion of the channel. The roughness-covered plates ($\sim 1.5\,m$) form the top and bottom walls for the remainder of the test section. This results in a roughness fetch of $30H$ before the first tap used in the determination of dp/dx. In a previous work (Flack et al., 2016), fully-developed flow was confirmed with velocity profiles located $90H$ and $110H$ downstream of the trip. Details of the velocity measurements are outlined in Schultz and Flack (2013).

The rough surfaces investigated in this work were created mathematically with the desire to achieve full control of the surface parameters. That is, surface statistics, such as *r.m.s*, *peak-to-trough height*, *skewness* and *kurtosis*, can be systematically changed and controlled. This methodology opens the possibility to better identify the roughness scales that contribute the most to frictional drag, as well as the onset to the transitionally- and fully-rough regimes. The surfaces were generated in MATLAB using a circular Fast Fourier Transform (FFT) with a random set of independent phase angles, distributed between 0 and 2π, with a power-law slope transfer function, $H = \kappa^P$, where κ is the wavenumber and P the slope of the power-law. This approach is similar to the one used by Anderson and Meneveau (2011). Therefore, the roughness generated by this method contains a multitude of scales that obeys the imposed power-law slope power spectrum ($E(\kappa) \sim \kappa^P$), and the surface elevation possesses a Gaussian probability-density-function ($p.d.f$). For the surface roughness tested in this work, the slope of the power law was systematically changed while holding the amplitude constant. Table 1 summarizes the surface statistics of the three tested surfaces, $P = -0.5, -1.0$ and -1.5, which includes the roughness *r.m.s*, k_{rms}, peak-to-trough height, k_t, mean elevation, k_a, skweness, Sk, kurtosis, Ku, effective slope, ES (Napoli et al., 2008), and the equivalent sang-grain roughness height, k_s. The generated surfaces were then reproduced using a high-resolution 3D printer (Projet 3500 HDMax, with lateral resolution $34\,\mu$m, elevation resolution $16\,\mu$m). Due to the complexity of these rough surfaces and limitations of the printer's software, the maximum roughness tile that could be successfully printed, with a spatial resolution of $40\,\mu$m, was $\sim 108\,\text{mm} \times 108\,\text{mm}$ [1]. This required the concatenation of multiple printed roughness patches in order to cover the entire width of the channel. To efficiently replicate the printed rough surfaces, a mold/cast technique was employed. A composite panel, comprised of four printed roughness tiles and arranged in a two by two array, for each power-law slope investigated herein, was created. To avoid any secondary flow, these four smaller tiles had the exact same roughness statistics, however, each of which with different random phases, and therefore with different topographical features. The tiles were glued using epoxy (West System 105 with a 206 Slow Hardener) onto a piece of G-10 using vacuum-bagging technique to ensure flatness of the tiles. The procedure consisted of creating silicon rubber molds (Smooth-On Mold Star 30) from a composite roughness panel. The rubber mix was de-gassed to get rid of all the bubbles that could deprecate the quality of the roughness textures. Half-way through pouring the mix onto the composite panel, the molds were reinforced with two layers of carbon fiber (covering the entire size of the mold) to minimize any distortions and shrinkage in order to ensure that all roughness tiles had the same dimensions. The roughness tiles were reproduced using epoxy (West System 105 with a 206 Slow Hardener) as the cast material. Great care was taken when pouring the mix onto the silicon rubber mold to avoid any bubbles becoming stuck on the rough surface. A total of 20 tiles were reproduced per power-law slope. Once the casting was concluded, the tiles were glued onto a piece of acrylic (two of $\sim 216\,\text{mm} \times 1525\,\text{mm}$) using the same epoxy and the vacuum bagging technique. This assured that all tiles were perfectly flush onto the acrylic plate. Subsequently, these plates were machined using a 5-axis milling station (Hass VF-11), placed on a vacuum table, to the size specification to fit in the channel flow facility.

The surfaces scans, comprised of 50 mm by 15 mm (x and y direction, respectively), were obtained with an optical profilometer utilizing white light interferometry (Veeco Wyco NT9100), with sub-micron vertical resolution and 3.4μm of lateral resolution. Figure 1(left-panel) shows the contour maps of the investigated surfaces measured by the profilometer. The data acquired from the profilometer require careful post-processing in order to remove any anomalies and spurious data as well as filling all holes in the surface scans. The surface scans had tilt and curvature removed, and the holes were filled using a PDE-based interpolation method (Bertalmio et al., 2000). Spurious data from the interpolation step were removed by a median-test filter, followed by a second PDE-based interpolation. Further details of the post-processing can be found in Flack et al. (2016). In order to compute the roughness statistics, a total of 10 line-scans per surface were extracted (x - direction). These profiles had 1 mm space between them to ensure statistical independence.

2.1. Uncertainty estimates

Uncertainty estimates in the measured quantities presented herein were calculated using the method of Moffat (1988) which accounts for both precision and bias, following the procedure used by Flack et al. (2016). In summary, the precision uncertainty in the skin-friction was calculated at 95% confidence by multiplying the standard error by the two-tailed t-value as described in Coleman and Steele (1995). The standard errors were calculated from the results of six replicate experiments covering the entire Reynolds number range. Bias estimates were combined

[1] Extensive qualitative and quantitative comparison analyses were performed between the generated surfaces and their printed counterparts. Roughness statistics differences were verified to be no more than 10-15 μm in the k_{rms}.

© 2018

This work is licensed under a Creative Commons "Attribution-NonCommercial-NoDerivatives 4.0 International" license.

Table 1: Roughness statistics, *i.e.*, k_a, k_{rms}, k_t, Sk, Ku, and ES, for the tested surfaces.

$E(\kappa) \sim \kappa^P$	$k_a[\mu m]$	$k_{rms}[\mu m]$	$k_t[\mu m]$	Sk	Ku	ES	$k_s[\mu m]$
$P = -0.5$	21.0	25.9	73.3	0.11	2.9	0.14	53.0
$P = -1.0$	25.3	31.1	84.9	0.08	2.9	0.12	33.5
$P = -1.5$	24.3	40.4	104.2	-0.03	2.9	0.09	21.0

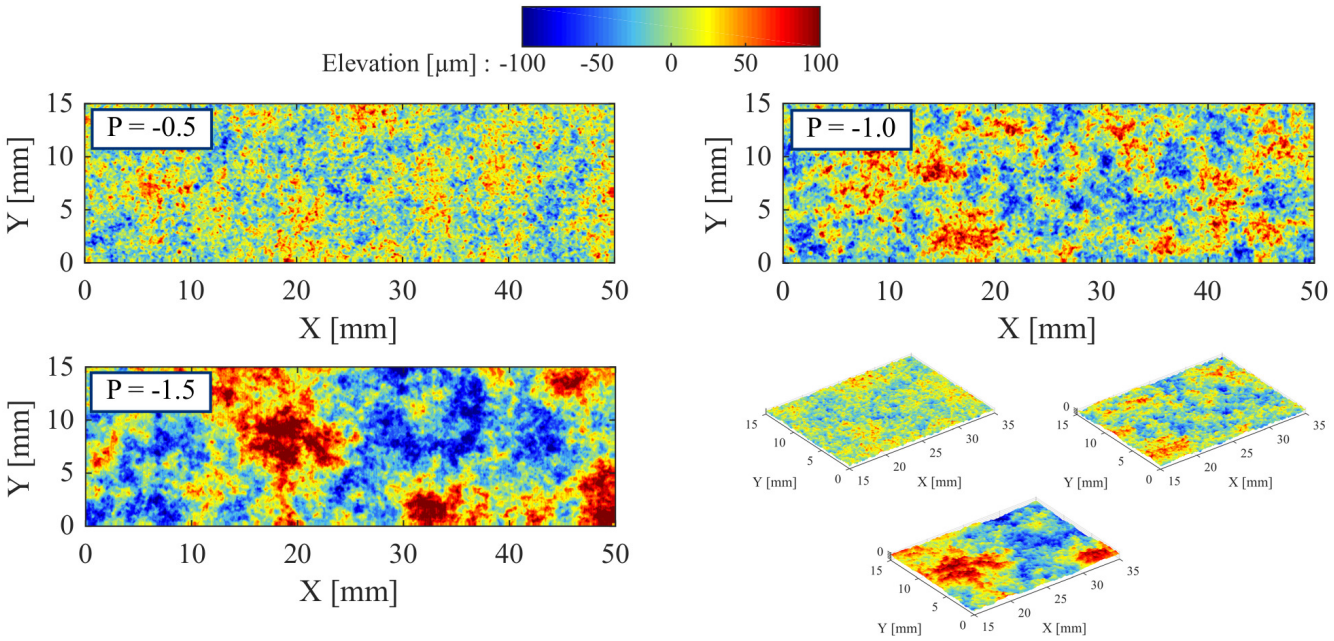

Figure 1: Contour maps of the printed version from the mathematically generated rough surfaces with power law slopes $P = -0.5$, -1.0 and -1.5. Lower-right corner depicts isometric view of the 3 surfaces. Height was multiply by 3 to emphasis the topography.

with the precision uncertainties to calculate the overall uncertainties in the skin-friction. The overall uncertainty in C_f is typically $\pm 9\%$ at the lowest Reynolds number ($Re_m = 11,000$) but rapidly drops to about $\pm 1.2\%$ for $Re_m \geq 40,000$. The uncertainty in the roughness function was calculated using standard error propagation techniques. The uncertainties in C_f outlined above were propagated through Eq. 4. The resulting overall uncertainty in U^+ is $\pm 3.8\%$ or ± 0.15, whichever is greater.

3. Results and Discussion

The skin-friction, C_f, results for all the tested surfaces as a function of Reynolds number, Re_m are shown in figure 2. Also shown are the smooth wall experimental results of Schultz and Flack (2013) for comparison. At lower Reynolds number, all surfaces are hydraulically-smooth. Furthermore, at sufficiently high Reynolds number the surfaces exhibit fully-rough behavior, where the skin-friction becomes independent of Reynolds number. It is also worth pointing out that the C_f curves presented herein do not seem to have the Nikuradse-like inflectional behavior in the transitionally-rough regime (Nikuradse, 1933). Surface 1 ($P = -0.5$) produces the highest frictional drag, whereas surface 3 ($P = -1.5$) has the lowest drag. This is an interesting result, because as the power-law slope, P, becomes steeper the surface tends to produce less drag. This seems counterintuitive if one only draws a conclusion regarding the drag from the surfaces' statistics (table 1) and surface topography maps (figure 1). In fact, it is clear that the surface with the power-law slope of $P = -1.5$ has the largest statistical and topographical features, whereas the surface with the slope of $P = -0.5$ has the least. Conversely, table 1 shows that the equivalent roughness grain height, k_s, for $P = -0.5$ is $k_s = 53.0\mu$m (most drag), and $k_s = 21.0\mu$m for $P = -1.5$ (least drag). These results from the skin-friction seem to indicate that there are roughness scales that do not contribute significantly to the drag.

The roughness function, ΔU^+, for a range of roughness Reynolds number, k_s^+, where k_s is the equivalent sand grain roughness height, is shown in figure 3. A similarity-law procedure of Granville (1987) for fully-developed internal flows was employed to determine the roughness function, ΔU^+ (Eq. 4). In the fully-rough regime the roughness function for all the tested surfaces display good collapse, as expected, when scaled with using k_s. The onset to the transitionally-rough regime seems to be a function of the power-law slope, P, where it varies from $k_s^+ \sim 0.7$

© 2018

This work is licensed under a Creative Commons "Attribution-NonCommercial-NoDerivatives 4.0 International" license.

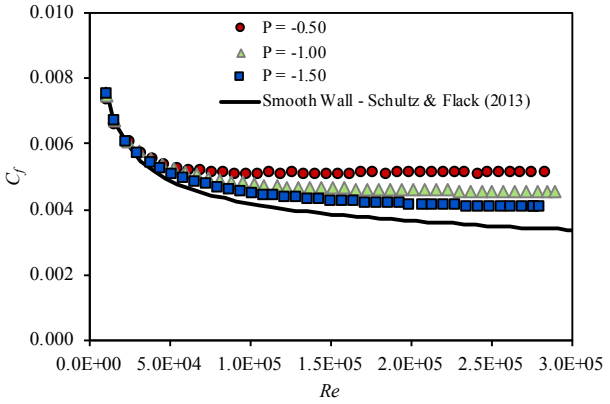

Figure 2: Skin-friction coefficient across Reynolds number. Symbols are: ● for $P = -0.5$; ▲ for $P = -1.0$; ■ for $P = -1.5$; and — for smooth-wall Schultz and Flack (2013)

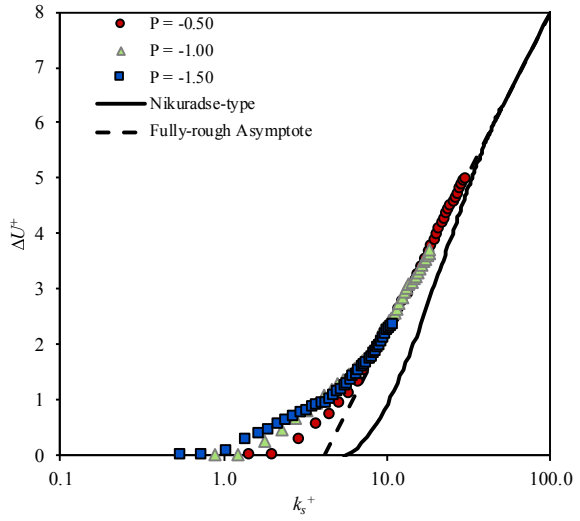

Figure 3: Roughness function *versus* the equivalent sand grain roughness height, k_s^+. Symbols are: ● for $P = -0.5$; ▲ for $P = -1.0$; ■ for $P = -1.5$.

for $P = -1.5$ to $k_s^+ \sim 2$ for $P = -0.5$. Additionally, the onset of the fully-rough regime occurs from $k_s^+ \sim 10$ to $k_s^+ \sim 15$, and it also seems to be a function of the power-law slope. Therefore, the rough surfaces tested in this work display notable variation in the transitionally-rough regime. This is particularly interesting because in a previous study from Flack et al. (2016) it was found that the different grit-blasted surfaces did not display significant variations in the transitionally-rough regime. In fact, the roughness function remained relatively invariant with surface texture. This may have to do with the fact that these grit-blasted surfaces are inherently negatively skewed. It is important to remember that the surfaces tested in the present work have a Gaussian *p.d.f* ($Sk \sim 0$; $Ku \sim 3$). Therefore, it could be that skewness may play an important role in the overall behavior of the roughness function in the transitionally-rough regime. Similarly to the C_f curves shown in figure 2, the shape of the roughness function in the transitionally-rough regime does not follow the Nikuradse (1933) roughness function for uniform sand grain. Additionally, it does not follow the Colebrook et al. (1939) roughness function that is used in the Moody diagram (Moody, 1944).

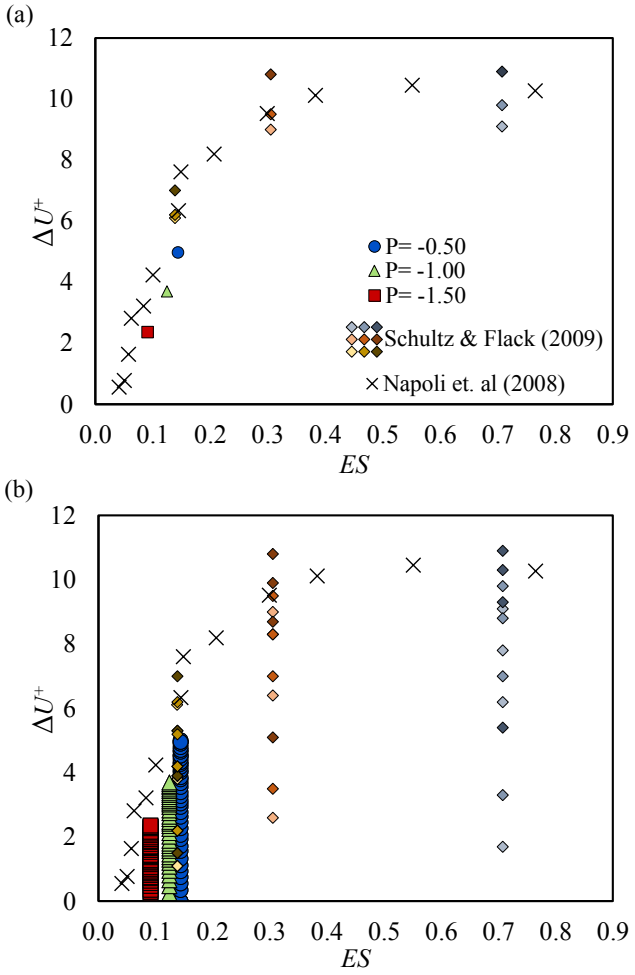

Figure 4: Effective slope, ES, *versus* roughness function, ΔU^+, for the tested surfaces (● for $P = -0.5$; ▲ for $P = -1.0$; ■ for $P = -1.5$), (a) Highest Reynolds number, and (b) Reynolds number dependency. Also included Napoli et al. (2008) (× symbols), and Schultz and Flack (2009) (colored ◊ symbols)

As previously mentioned, it seems that there may be some roughness scales, mainly in the $P = -1.5$ and $P = -1.0$ cases, that do not significantly contribute to frictional drag. Referring back to figure 1, one could naively draw conclusions regarding the impact each of surfaces tested herein have on the drag by simply looking at their topographical features, i.e. how rough they are. Figure 4(a) shows the correlation between the effective slope, ES, and the roughness function for the tested roughness. Additionally, data from Napoli et al. (2008) and Schultz and Flack (2009) are included for comparison. It can be seen that the surface roughness investigated in this work fall below the value where the roughness function is independent of the effective slope, $ES \geq 0.35$. This means that the tested roughness fall under the so-called "wavy" regime (Schultz

© 2018

This work is licensed under a Creative Commons "Attribution-NonCommercial-NoDerivatives 4.0 International" license.

and Flack, 2009). The implication of this factor is that long wavelength roughness scales may not play an important role in generating drag. More specifically, the lower the effective slope the more long-wavelength range that will not contribute to the frictional drag. This fact causes the surface roughness to reach a lower roughness function value (as seen by Napoli et al. (2008)). From figure 4, it can be seen that the surface $P = -0.5$ has the highest effective slope ($ES = 0.14$) value and $P = -1.5$ has the lowest ($ES = 0.09$). This may help explain why the surface with power-law slope of $P = -0.5$ produces higher drag than the surface with the slope of $P = -1.5$, where, clearly, the latter possesses more dominant long wavelength roughness scales.

In fact, Schultz and Flack (2009) pointed out that for surfaces with $ES \leq 0.35$ the roughness height does not provide a good scale for the roughness function. This may help explain why the surface with power-law slope of $P = -0.5$ produces higher drag than the surface with the slope of $P = -1.5$, where, clearly, the latter possesses more dominant long wavelength roughness scales. Additionally, it is worth noting that effective slope has a Reynolds number dependency, as depicted in figure 4(b) (data available for the current work and Schultz and Flack (2009)).

It is, therefore, important to identify which scales are contributing more to the generation of frictional drag. In order to determine the threshold of which of the longer wavelength scales start to not have a significant role on the drag, a high-pass filter was applied on the profiled surface data for all the three tested rough surfaces. To determine the size of the filter, the R^2 value was computed from a linear least-square fit between high-pass filtered roughness root-mean-square, k_{rms}, and k_s, for a range of filter size (from 0.1 mm to 10 mm). This resulted in an optimal filter size of 1 mm (highest R^2 value), where these values is approximately 10 times higher than the largest surface statistic (roughness peak-to-trough height, k_t for the $P = -1.5$). Subsequently, the roughness statistics were computed for this filter size, which the filtered roughness statistics can be found in table 2. Figure 5a shows the correlation between k_{rms} and k_s for both unfiltered and with a 1 mm high-pass filter applied. It is clear that, for the unfiltered roughness statistics (red), the correlation between k_{rms} and k_s has an opposite trend when compared with the k_s trend (table 1). That is, when k_s is higher, i.e. more drag, k_{rms} is smaller. This is clearly counterintuitive. Moreover, as expected, other roughness statistics, namely, peak-to-trough height k_t (figure 5b) and roughness average height k_a (figure 5c) show the same opposite correlation trend. Conversely, when a 1 mm high-pass filter was applied to the tested surfaces, the correlation between k_{rms} and k_s has the correct trend. That is, when k_{rms} becomes higher k_s also increases (blue; figure 5a). The same trend can be observed for other surface statistics, k_a, the average roughness height, and k_t, the peak-to-though roughness height, as shown in figure 5b 5c. Interestingly, the values of ES for both unfiltered and 1 mm high-pass filtered surfaces remain relatively unchanged (figure 6). This means that ES is quite insensitive to high-pass filtering, and thus a potential robust parameter candidate for future roughness models. In fact, Chan et al. (2015) developed a model for ΔU^+ as a function of solely k_a^+ (normalized in inner wall units) and ES from DNS over 3D sinusoidal-type roughness. The data from Napoli et al. (2008); Yuan and Piomelli (2014) and Schultz and Flack (2009) were also used in this model resulting in a good agreement with the measured ΔU^+.

The model proposed by Flack and Schultz (2010) was employed for both the unfiltered and 1 mm high-pass filtered statistics, as shown in figure 7. It can be seen that the model provides the same correct trend for both statistics. However, the determined coefficients are vastly different. Although, the coefficients for the filtered statistics data more closely match the ones determined in Flack and Schultz (2010). It is worth noting that the 1 mm high-pass filter fit provides a better R^2. Moreover, ideally, more roughness data are needed to fully assess this model in the so-called "wavy-regime". However, as a first order analysis this result further emphasizes the necessity of surface filtering in order to identify the scales that contribute most significantly to the frictional drag.

Finally, to qualitatively demonstrate the effect of the high-pass filter has on the tested surfaces, figure 8 depicts the contour maps of the measured roughness, where the left panel shows the original, unfiltered data from the profilometer (with both curvature and tilt removed) and the right panel shows the surfaces in which the 1 mm high-pass filter was applied. Focusing on the high-pass filtered contour maps (right panel), it can be seen that surface with $P = -0.5$ has the most topographical features, whereas the surface with $P = -1.5$ has the least features, with surface $P = -1.0$ siting in between. As expected, this qualitatively result has the exact trend seen on the frictional drag curves (figure 2). It is particularly interesting to see what roughness scales are contributing to the frictional drag, which provides a link between the trends seen in the C_f curves coupled with the justification for filtering the surfaces based on the fact that their effective slope values fall in the "wavy" regime with $ES \leq 0.35$.

4. Summary

Results are presented for three rough surfaces with a range of scales following a power-law slope of $P = -0.5$, -1.0 and -1.5. Skin-friction for all tested surfaces display fully-rough behavior and the entire roughness function is mapped to determine the extent and shape of ΔU^+ in the transitionally-rough regime. Interestingly, the surface with power law slope $P = -0.5$ generates the most drag even though this surface has the smallest roughness features as determined from surface statistics. As the power law slope increases, the drag imposed by the surface is reduced. This emphasizes that some surface wavelengths are not significantly contributing to the drag. These are likely

© 2018

This work is licensed under a Creative Commons "Attribution-NonCommercial-NoDerivatives 4.0 International" license.

Table 2: Roughness statistics of the tested surfaces after applying a 1mm high-pass filter.

$E(\kappa) \sim \kappa^P$	$k_a[\mu m]$	$k_{rms}[\mu m]$	$k_t[\mu m]$	Sk	Ku	ES	$k_s[\mu m]$
$P = -0.5$	9.6	12.1	37.5	0.16	3.1	0.13	53.0
$P = -1.0$	8.3	10.5	32.7	0.21	3.2	0.11	33.5
$P = -1.5$	5.5	7.0	23.9	0.04	3.2	0.08	21.0

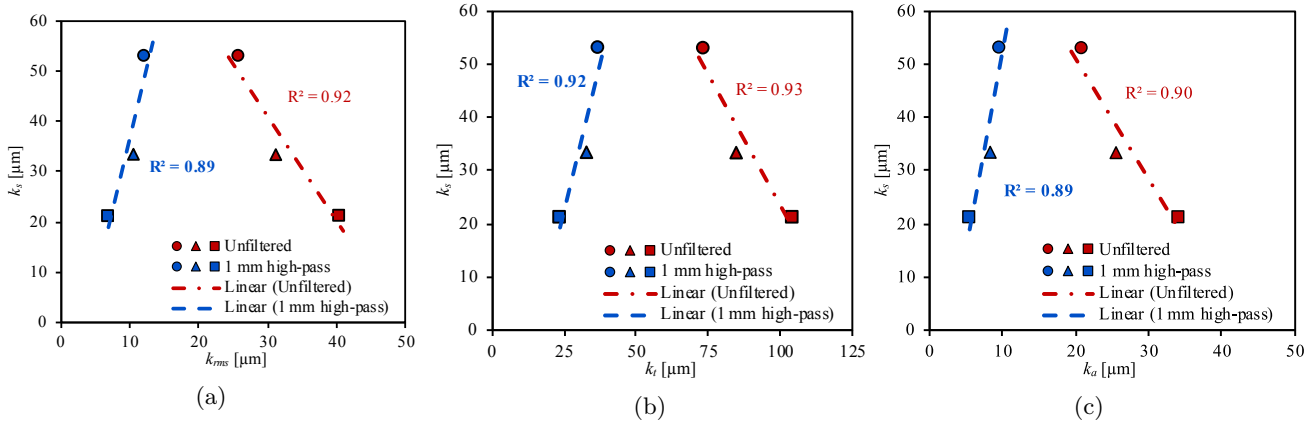

Figure 5: Correlation of k_{rms}(a), k_t(b), and k_a(c) with respect to the measured k_s for unfiltered (red) and for 1 mm high-pass filter (blue). Symbols represent the power-law slope of the tested surfaces: ◯ for $P = -0.5$; △ for $P = -1.0$; and □ for $P = -1.5$.

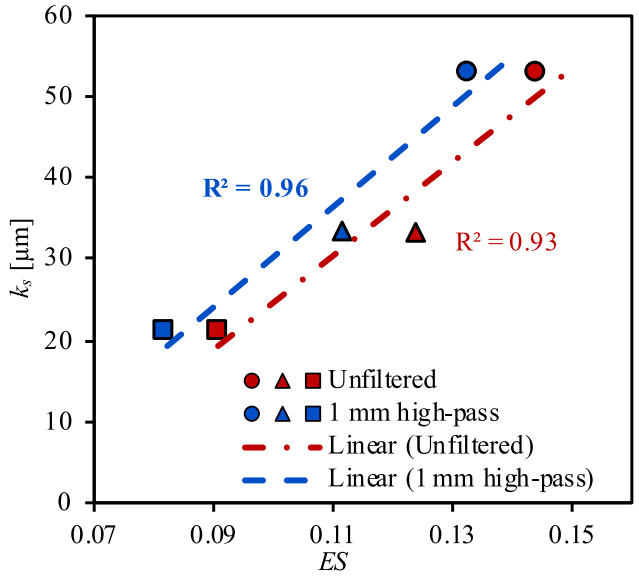

Figure 6: Correlation between ES and k_s for unfiltered (red) and for 1 mm high-pass filter (blue). Symbols represent the power-law slope of the tested surfaces: ◯ for $P = -0.5$; △ for $P = -1.0$; and □ for $P = -1.5$.

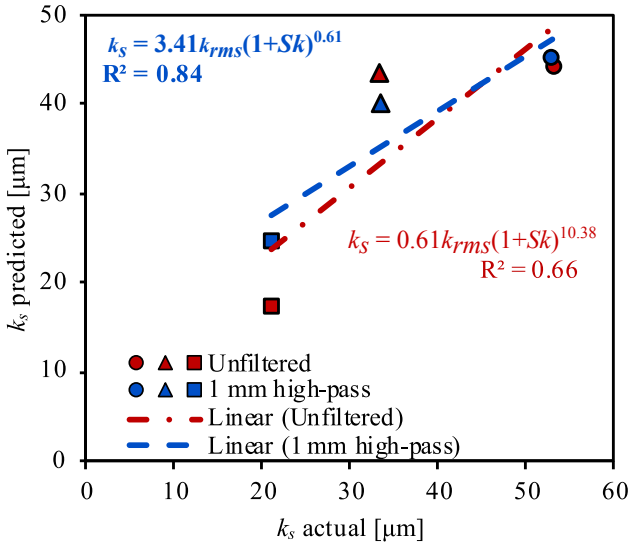

Figure 7: Correlation between k_s actual and k_s predicted by Flack and Schultz (2010) model for unfiltered (red) and for 1 mm high-pass filter (blue). Symbols represent the power-law slope of the tested surfaces: ◯ for $P = -0.5$; △ for $P = -1.0$; and □ for $P = -1.5$.

the undulating, wavy surface features. In fact, the ES of all the surfaces fall under the so-called "wavy" regime. These results highlight the need for high-pass filtering in the determination of predictive correlations for frictional drag, which produce the correct trend between k_s and k_{rms}.

To the authors knowledge, this study is the first to experimentally measure the frictional drag on mathematically generated roughness with surface statistics parametrically altered. While results from only three surfaces are presented, the technique and methodology are significant for planned future studies and follow-on work with a wider range of surface parameters. The method of producing the surface roughness is also important since results can be used to validate computational models of flow over rough surfaces. It is expected that a much wider range or surface statistics can be investigated using DNS. It is hoped that the combined experimental and computational efforts will

© 2018

This work is licensed under a Creative Commons "Attribution-NonCommercial-NoDerivatives 4.0 International" license.

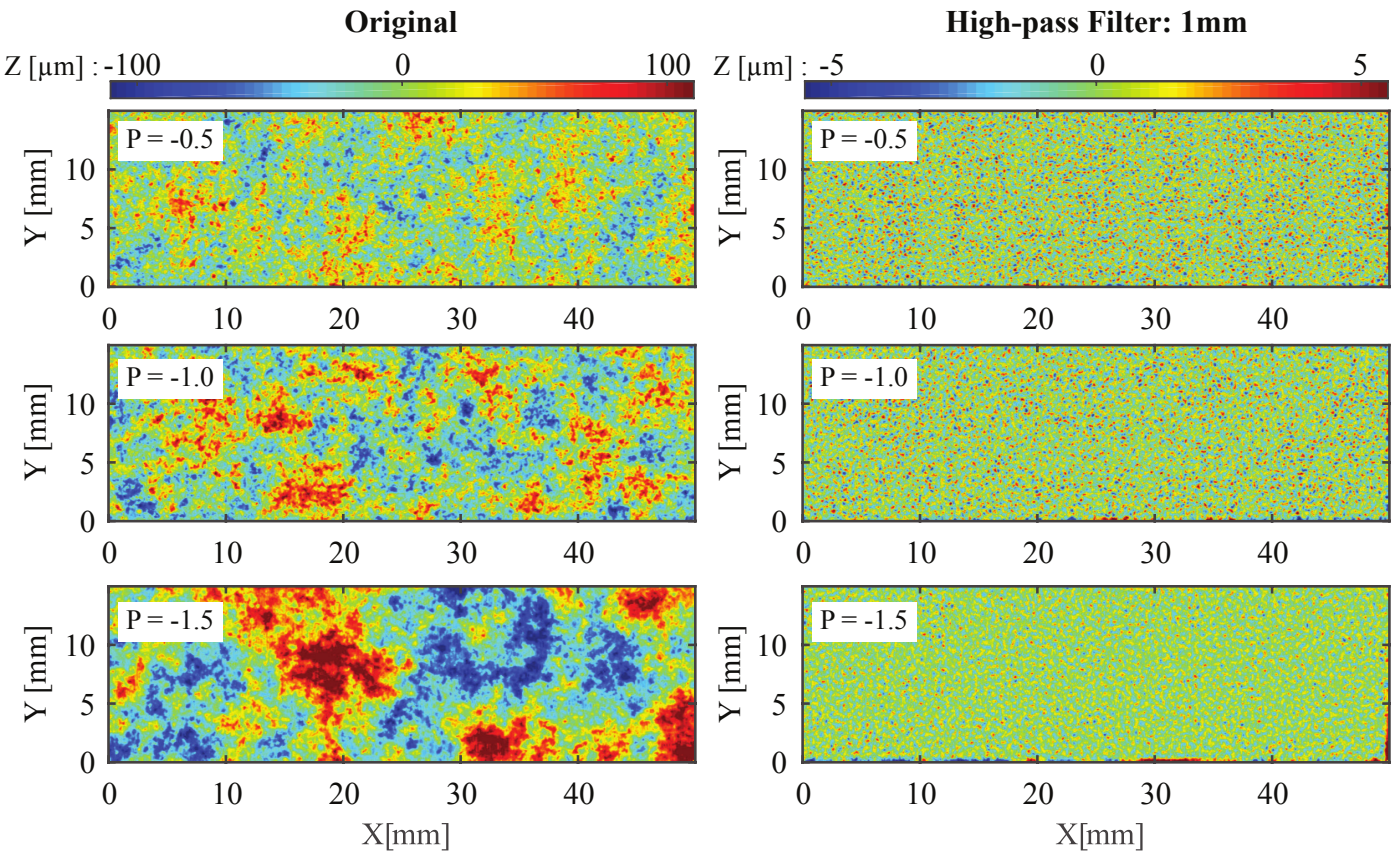

Figure 8: Contour maps of digital scans for all three tested surface roughness. Left panel shows the surfaces without filtering, whereas the right panel shows the surfaces with a 1 mm high-pass filter.

advance the study of rough wall flows and produce robust engineering correlations for the prediction of friction drag.

5. Acknowledgements

The authors would like to thank the Office of Naval Research for providing financial support and the United States Naval Academy Hydromechanics Laboratory for providing technical support.

References

Anderson W, Barros JM, Christensen KT, Awasthi A. Numerical and experimental study of mechanisms responsible for turbulent secondary flows in boundary layer flows over spanwise heterogeneous roughness. Journal of Fluid Mechanics 2015;768:316–47.

Anderson W, Meneveau C. Dynamic roughness model for large-eddy simulation of turbulent flow over multiscale, fractal-like rough surfaces. Journal of Fluid Mechanics 2011;679:288–314.

Barros JM, Christensen KT. Observations of turbulent secondary flows in a rough-wall boundary layer. Journal of Fluid Mechanics 2014;748:R1.

Bertalmio M, Sapiro G, Caselles V, Ballester C. Image inpainting. In: Proceedings of the 27th Annual Conference on Computer Graphics and Interactive Techniques. ACM Press/Addison-Wesley Publishing Co.; 2000. p. 417–24.

Bettermann D. Contribtion a L'etude de la Couche Limite Turbulent le Long de Plaques Regueuses. Technical Report 65-6; Center National de la Recherche Scientifique; 1965.

Chan L, MacDonald M, Chung D, Hutchins N, Ooi A. A systematic investigation of roughness height and wavelength in turbulent pipe flow in the transitionally rough regime. Journal of Fluid Mechanics 2015;771:743–77.

Colebrook CF, Blench T, Chatley H, Essex E, Finniecome J, Lacey G, Williamson J, Macdonald G. Correspondence. turbulent flow in pipes, with particular reference to the transition region between the smooth and rough pipe laws.(includes plates). Journal of the Institution of Civil engineers 1939;12(8):393–422.

Coleman HW, Steele WG. Engineering application of experimental uncertainty analysis. AIAA journal 1995;33(10):1888–96.

Dirling Jr R. A method for computing roughwall heat transfer rates on reentry nosetips. In: 8th Thermophysics Conference. 1973. p. 763.

Dvorak F. Calculation of turbulent boundary layers on rough surfaces in pressure gradient. AIAA journal 1969;7(9):1752–9.

Flack KA, Schultz MP. Review of hydraulic roughness scales in the fully rough regime. Journal of Fluids Engineering 2010;132(4):041203.

Flack KA, Schultz MP, Barros JM, Kim YC. Skin-friction behavior in the transitionally-rough regime. International Journal of Heat and Fluid Flow 2016;61:21–30.

Granville PS. The frictional resistance and turbulent boundary layer of rough surfaces. Journal of Ship Resistance 1958;2:52–74.

Granville PS. Three indirect methods for the drag characterization of arbitrarily rough surfaces on flat plates. In: Proceedings of the Twenty-first American Towing Tank Conference. National Academies; 1987. p. 117.

Kevin K, Monty JP, Bai HL, Pathikonda G, Nugroho B, Barros JM, Christensen KT, Hutchins N. Cross-stream stereoscopic particle image velocimetry of a modified turbulent boundary layer over directional surface pattern. Journal of Fluid Mechanics

© 2018

This work is licensed under a Creative Commons "Attribution-NonCommercial-NoDerivatives 4.0 International" license.

2017;813:412–35. doi:10.1017/jfm.2016.879.

Macdonald R, Griffiths R, Hall D. An improved method for the estimation of surface roughness of obstacle arrays. Atmospheric Environment 1998;32(11):1857–64.

Moffat RJ. Describing the uncertainties in experimental results. Experimental thermal and fluid science 1988;1(1):3–17.

Moody LF. Friction factors for pipe flow. Trans Asme 1944;66(8):671–84.

Napoli E, Armenio V, De Marchis M. The effect of the slope of irregularly distributed roughness elements on turbulent wall-bounded flows. Journal of Fluid Mechanics 2008;613:385–94.

Nikuradse J. Laws of flow in rough pipes. NACA Technical Memorandum 1292 1933;.

Nugroho B, Hutchins N, Monty J. Large-scale spanwise periodicity in a turbulent boundary layer induced by highly ordered and directional surface roughness. International Journal of Heat and Fluid Flow 2013;41:90–102.

Schultz MP, Flack KA. Turbulent boundary layers on a systematically varied rough wall. Physics of Fluids 2009;21(1):015104.

Schultz MP, Flack KA. Reynolds-number scaling of turbulent channel flow. Physics of Fluids 2013;25(2):025104.

Willingham D, Anderson W, Christensen KT, Barros JM. Turbulent boundary layer flow over transverse aerodynamic roughness transitions: induced mixing and flow characterization. Physics of Fluids 2014;26(2):025111.

Yang XI, Sadique J, Mittal R, Meneveau C. Exponential roughness layer and analytical model for turbulent boundary layer flow over rectangular-prism roughness elements. Journal of Fluid Mechanics 2016;789:127–65.

Yuan J, Piomelli U. Estimation and prediction of the roughness function on realistic surfaces. Journal of Turbulence 2014;15(6):350–65.

© 2018

This work is licensed under a Creative Commons "Attribution-NonCommercial-NoDerivatives 4.0 International" license.